Check for updates

Covalent organic frameworks based on tetraphenyl-*p*-phenylenediamine and metalloporphyrin for electrochemical conversion of CO$_2$ to CO†

Lei Gong,[a] Baotong Chen,[a] Ying Gao,[a] Baoqiu Yu,[a] Yinhai Wang,[a] Bin Han,[a] Chenxiang Lin,[b] Yongzhong Bian, [ID] *[a,c] Dongdong Qi*[a] and Jianzhuang Jiang [ID] *[a,c]

Electrocatalytic CO$_2$ reduction provides a possible method for carbon neutralization. Electrode materials with efficient electron transfer, high selectivity and large current density are highly desirable. Herein, we have developed a couple of tetraphenyl-*p*-phenylenediamine and metalloporphyrin-based 2D COFs for the electrocatalytic CO$_2$ reduction. TPPDA-MPor-COFs (M = Co and Ni) were obtained by the cross-condensation of tetraphenyl-*p*-phenylenediamine (TPPDA) and 5,10,15,20-tetrakis(4-formylphenyl)-metalloporphyrin (MPor). The as-prepared TPPDA-CoPor-COF shows high CO faradaic efficiencies of 87–90% from −0.6 to −0.9 V *vs.* RHE, and the largest CO partial current density (j_{CO}) of TPPDA-CoPor-COF (−22.2 mA cm^{-2} at −1.0 V *vs.* RHE) exceeds those of most of the reported COF-based electrocatalysts. Notably, exfoliated TPPDA-CoPor-COF nanosheets (TPPDA-CoPor-COF-NSs) show much better electrocatalytic performance. The CO faradaic efficiencies of TPPDA-CoPor-COF-NSs are over 90% in a wider voltage range (−0.7 to −0.9 V), and the maximum j_{CO} reaches up to −29.2 mA cm^{-2} at −1.0 V. Density functional theory calculations have been performed to rationalize the improved CO$_2$RR performance of TPPDA-CoPor-COF.

Introduction

In order to achieve carbon neutralization, photocatalysis,[1–3] electrocatalysis[4–6] and thermal catalysis[7] have been developed over the past decades. The electrocatalytic CO$_2$ reduction reaction (CO$_2$RR) is considered as a promising strategy among them, which is clean and mild and can be associated with renewable energy.[8,9] Varieties of homogeneous and heterogeneous catalysts have been developed for the efficient and selective electrocatalytic CO$_2$RR.[10–17] Although homogeneous catalysts have been proved to show low overpotential and high selectivity by means of smart design and functional group regulation,[11] inefficient electron transfer and poor stability in homogeneous organic catalytic systems restrain their practical application. Meanwhile, due to their aqueous compatibility and great catalytic activity, various heterogeneous catalysts have been investigated.[18,19]

As promising porous crystalline materials, metal–organic frameworks (MOFs)[20–22] and covalent organic frameworks (COFs)[23,24] have been explored for the electrocatalytic CO$_2$RR. In particular, the building blocks of COFs can be manipulated precisely for specific activity and selectivity. Some active homogeneous molecular catalysts, such as porphyrins[25–31] and phthalocyanines,[32–34] could be integrated into COFs as building blocks for the electrocatalytic CO$_2$RR. Nevertheless, most of the reported COF materials exhibit limited current density and relatively low faradaic efficiency. Hence, novel COFs with high current density and excellent energy conversion efficiency are highly desirable.

Tetraphenyl-*p*-phenylenediamine, as a typical electron donor, has a high electron transfer capability and has been widely used in preparing electrochemically active materials.[35–39] On the other hand, metalloporphyrins (MPor) can function as excellent electron acceptors and charge transfer components due to their conjugated macrocyclic structures.[27–29,40–42] Therefore, efficient intramolecular electron transfer paths might be constructed by integrating TPPDA

[a]*Beijing Key Laboratory for Science and Application of Functional Molecular and Crystalline Materials, Department of Chemistry, School of Chemistry and Biological Engineering, University of Science and Technology Beijing, Beijing 100083, China. E-mail: yzbian@ustb.edu.cn, qdd@ustb.edu.cn, jianzhuang@ustb.edu.cn*
[b]*Guangxi Key Laboratory of Natural Polymer Chemistry and Physics, Nanning Normal University, Nanning 530001, China*
[c]*Daxing Research Institute, and Beijing Advanced Innovation Center for Materials Genome Engineering, University of Science and Technology Beijing, Beijing 100083, China*
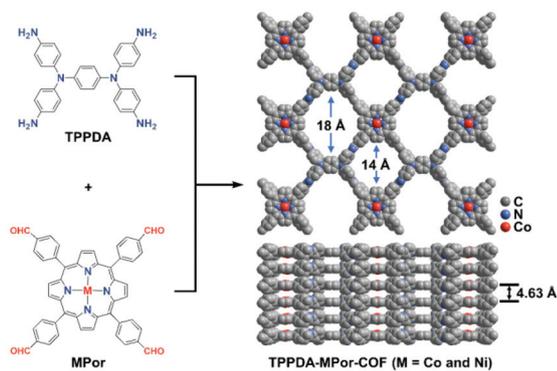†Electronic supplementary information (ESI) available: Experimental section and additional figures and tables. See DOI: https://doi.org/10.1039/d2qi00336h

This journal is © the Partner Organisations 2022

Inorg. Chem. Front., 2022, **9**, 3217–3223 | **3217**

Fig. 1 The synthesis of TPPDA-MPor-COFs (M = Co and Ni).

and MPor into two-dimensional COFs, and enhanced electrocatalytic CO_2RR activities are expected for the obtained COFs.

Herein, MPor and TPPDA-based COFs (TPPDA-MPor-COFs, M = Co(II) and Ni(II)) have been synthesized for the first time (Fig. 1). TPPDA-CoPor-COF exhibits high CO faradaic efficiencies (FE_{CO}) and large CO partial current densities (j_{CO}), which can be further improved by physical ultrasonic exfoliation. The obtained TPPDA-CoPor-COF nanosheets (TPPDA-CoPor-COF-NSs) show a maximum FE_{CO} of 92% at −0.7 V and a j_{CO} of −29.2 mA cm^{-2} at −1.0 V *vs.* RHE. The excellent electrocatalytic properties can be attributed to the large amount of accessible Co(II) sites and efficient electron transfer from TPPDA to CoPor blocks in these COF-based materials.

Results and discussion

Synthesis and characterization

TPPDA-MPor-COFs (M = Co and Ni) were synthesized *via* Schiff-base condensation of TPPDA and MPor (M = Co and Ni). The experimental powder X-ray diffraction (PXRD) patterns show that TPPDA-MPor-COFs have good crystallinity (Fig. 2a and S1†). Le Bail refinements of TPPDA-MPor-COFs were

carried out on the basis of experimental PXRD data (Fig. S2†).[43] Eclipsed (AA) and staggered (AB) stacking models of TPPDA-CoPor-COF were constructed, where the former one matches well with the experimental data. Furthermore, the refined results of TPPDA-CoPor-COF show low residual values (R_p = 5.04% and R_{wp} = 7.50%) indicating the validity of the AA stacking model. The unit cell information of TPPDA-CoPor-COF has been obtained as follows: triclinic $P1$ space group, a = 24.56 Å, b = 25.08 Å and c = 4.63 Å, α = 66.76°, β = 104.04°, γ = 90.83°. In the experimental PXRD pattern of TPPDA-CoPor-COF (Fig. 2a), the strong diffraction signals at 3.77°, 5.09° and 5.54° are assigned to the (100), (110) and (1−10) planes, respectively. A couple of weak signals at 10.20° and 11.12° are attributed to the (220) and (130) planes, respectively. TPPDA-NiPor-COF (Fig. S1†) shows similar PXRD results.

In the FT-IR spectra of TPPDA-MPor-COFs (Fig. 2b and S3†), the peaks at 1622 cm^{-1} reveal that the imine bond (C=N) formed successfully, along with a decrease of C=O (1699 cm^{-1}) and N–H (3458–3348 cm^{-1} and 1620 cm^{-1}) vibrations for MPor and TPPDA monomers, respectively.[44] In the solid-state electronic absorption spectrum, the characteristic absorptions of the MPor moiety (*i.e.* Q-band, 541 nm; sorbet band 432 nm) can be observed, suggesting the successful integration of the cobalt porphyrin unit into TPPDA-CoPor-COF (Fig. S4†).

The XPS spectra reveal the presence of C, N and Co/Ni elements in the two COFs (Fig. S5a and S6a†), and the two COFs show three characteristic peaks corresponding to the C–N (pyrrolic nitrogen) bond (398.6 and 398.7 eV) of MPor, and the C=N bond (399.0 and 399.1 eV) and the C–N bond (399.6 eV) of TPPDA, respectively (Fig. S5b and S6b†), further indicating the formation of the imine bond.[45] In addition, the XPS analyses of Co 2p and Ni 2p indicate that all the metal sites in TPPDA-MPor-COFs are divalent (Fig. S5c and S6c†).[46,47] The N_2 sorption curves of the two COFs display type I-isotherms (Fig. 2c and S8†). The adsorption curves show a steep increase when P/P_0 < 0.01, corresponding to the presence of permanent micropores. The Brunauer–Emmett–Teller (BET) surface area and the total pore volume of TPPDA-CoPor-COF were 1209 m^2 g^{-1} and 0.99 cm^3 g^{-1}, respectively (Fig. 2c). TPPDA-CoPor-COF displays two pore sizes (1.2 nm and 1.5 nm) (Fig. S7†), being consistent with the simulated structure (Fig. 1). TPPDA-NiPor-COF shows similar N_2 sorption and porous properties (Fig. S8† and S9†). Besides, TPPDA-CoPor-COF and TPPDA-NiPor-COF show moderate CO_2 sorption capacities of 26.8 cm^3 g^{-1} and 28.1 cm^3 g^{-1} at 25 °C and 1.0 bar, respectively (Fig. 2d and S10†), indicating the CO_2 affinity of TPPDA-MPor-COFs.

The scanning electron microscopy (SEM) and transmission electron microscopy (TEM) images show that TPPDA-MPor-COFs have layered morphologies with sizes of 100–500 nm (Fig. 3a, b and S11†). The element energy dispersive spectroscopy (EDS) mapping images (Fig. 3c and S12†) show the uniform distribution of metal ions (Co or Ni), C and N elements in TPPDA-CoPor-COF and TPPDA-NiPor-COF, respectively. The total Co content (3.35%) of TPPDA-CoPor-COF and Ni content (3.20%) of TPPDA-CoPor-COF were measured by
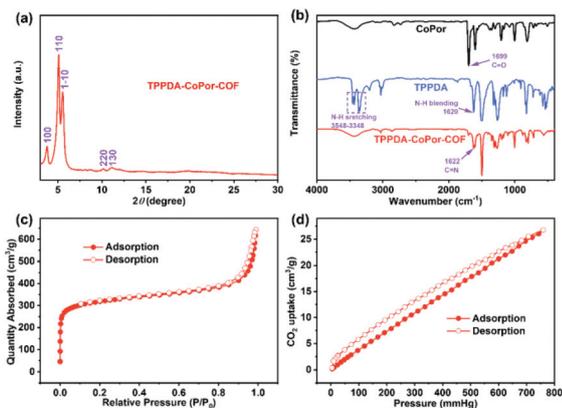

Fig. 2 (a) Experimental PXRD patterns, (b) FT-IR spectra, (c) N_2 sorption isotherm at 77 K and (d) CO_2 sorption isotherm at 298 K for TPPDA-CoPor-COF.
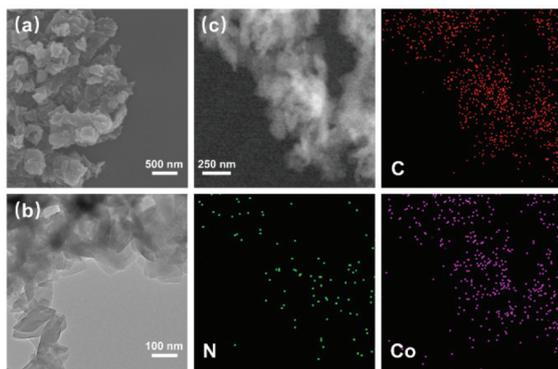
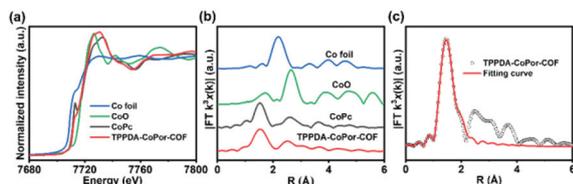Fig. 3 (a) SEM, (b) TEM and (c) EDS mapping images of TPPDA-CoPor-COF.

Fig. 4 (a) Co K-edge XANES spectra of TPPDA-CoPor-COF, CoPc, CoO and Co foil. (b) FT EXAFS spectra of TPPDA-CoPor-COF, CoPc, CoO and Co foil. (c) The EXAFS fitting curve of TPPDA-CoPor-COF.

Fig. 5 (a) LSV curves, (b) FEco, (c) j_{CO}, (d) TOF and (e) Tafel plots of TPPDA-MPor-COFs. (f) Lasting stability test for TPPDA-CoPor-COF at −0.8 V.

ICP tests (Table S1†), and are reasonably lower than the calculated metal contents. Thermal gravimetric analyses (TGAs) were carried out under a nitrogen atmosphere (Fig. S13†). TPPDA-MPor-COFs only displayed a slight weight loss till 500 °C owing to the loss of residual solvents, suggesting the high thermal stability of the COFs.

The Co K-edge XANES spectra of TPPDA-CoPor-COF and CoPc exhibit similar curves, suggesting that the coordination environment of Co atoms in TPPDA-CoPor-COF are the same as that of CoPc (Fig. 4a). In the Fourier-transform (FT) EXAFS curves, TPPDA-CoPor-COF displays a strong signal at 1.53 Å corresponding to the Co–N scattering path (Fig. 4b),[48] and no signal of Co–Co bonds was detected. EXAFS fitting for TPPDA-CoPor-COF was conducted using Co–N₄ coordination models. The result also suggests that the Co site in TPPDA-CoPor-COF is coordinated with four nitrogen atoms (Fig. 4c and Table S2†). TPPDA-NiPor-COF shows similar results (Fig. S14†).

Electrocatalytic performance

To investigate the catalytic performances of the COFs, a H-cell with a standard three-electrode system and 0.5 M KHCO₃ electrolyte solution was used. In order to avoid the accidental factors, three parallel experiments were conducted. All potentials are presented relative to the reversible hydrogen electrode (RHE) in this work.
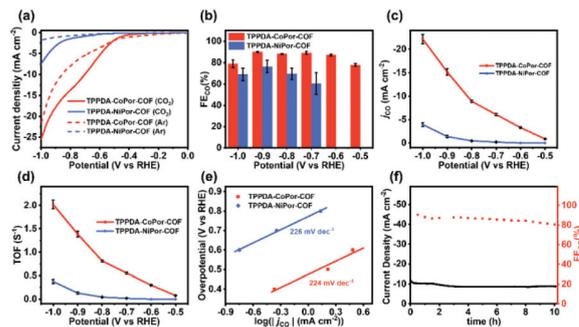
Linear sweep voltammetry (LSV) curves were obtained in CO₂ and Ar-saturated 0.5 M KHCO₃, respectively (Fig. 5a). The onset potential of TPPDA-CoPor-COF (−0.46 V) is more positive than that of TPPDA-NiPor-COF (−0.72 V). TPPDA-CoPor-COF also exhibits larger current densities in CO₂-saturated solution than in Ar-saturated solution from −0.5 to −1.0 V, suggesting greater electrocatalytic CO₂RR activity than the hydrogen evolution reaction (HER) activity. Short-term electrolysis tests and the corresponding gas chromatography analyses show that the products of the electrocatalytic CO₂RR were carbon monoxide and hydrogen (Fig. S15 and S16†). The nuclear magnetic resonance experiment shows that no liquid product is generated during the reduction process (Fig. S17†). Only a negligible amount of CO was detected when the control electrolysis was conducted in an Ar-saturated 0.5 M KHCO₃ electrolyte (Fig. S18†). Furthermore, carbon cloth decorated with Vulcan XC-72R carbon black and Nafion shows almost no electrocatalytic CO₂RR activity in the CO₂-saturated electrolyte (Fig. S19†). According to the above results, the source of CO and the electrocatalytic CO₂RR activity of TPPDA-CoPor-COF can be confirmed.

TPPDA-CoPor-COF exhibits high CO faradaic efficiencies (FE_CO) of 87–90% in the range of −0.6 to −0.9 V (Fig. 5b), while TPPDA-NiPor-COF shows lower FE_CO (i.e. 60–76% in −0.7 to −0.9 V). The j_{CO} values of TPPDA-CoPor-COF increase with elevated applied potential and reach up to −22.2 mA cm⁻² at −1.0 V, which is 5.7-fold that of TPPDA-NiPor-COF (−3.9 mA cm⁻²) (Fig. 5c) and surpasses most of the reported COFs (Fig. S20 and Table S3†). Moreover, in comparison with TPPDA-CoPor-COF, the maximum FE_CO of the CoPor monomer is only 76% at −0.8 V, and the maximum j_{CO} value is only −11.8 mA cm⁻² at −1.0 V (Fig. S21†), and the TPPDA monomer shows nearly 100% FE of H₂ in the range of −0.7 to −1.0 V (Fig. S22†). The above results indicate that the TPPDA unit plays an important role in promoting the electrocatalytic CO₂RR activity of TPPDA-CoPor-COF. Besides, the turnover frequency (TOF) of TPPDA-CoPor-COF was calculated to be 1.4 s⁻¹ at −0.9 V and 2.0 s⁻¹ at −1.0 V (Fig. 5d).

The Tafel slopes of TPPDA-CoPor-COF and TPPDA-NiPor-COF are tested to be 224 mV dec⁻¹ and 226 mV dec⁻¹, respect-

This journal is © the Partner Organisations 2022

Inorg. Chem. Front., 2022, 9, 3217–3223 | 3219

ively (Fig. 5e). The results imply the slightly superior reactivity of Co over Ni sites. The Nyquist plots of the electrochemical impedance test illustrate that TPPDA-CoPor-COF has a smaller charge-transfer resistance than TPPDA-NiPor-COF during the electrocatalytic CO_2RR process (Fig. S23†), confirming its more efficient electron transfer from the catalyst surface to the CO_2 molecules. To compare the electrochemically active surface areas (ECSAs) of TPPDA-MPor-COFs, electrochemical double-layer capacitances (C_{dl}) were acquired (Fig. S24†). TPPDA-CoPor-COF presents a C_{dl} value of 2.61 mF cm^{-2}, which is larger than 1.31 mF cm^{-2} for TPPDA-NiPor-COF, further indicating that TPPDA-CoPor-COF shows higher inherent catalytic activity.

Chronoamperometric tests were performed for TPPDA-CoPor-COF to evaluate the durability at −0.8 V in the H-cell. The corresponding FE_{CO} values remained higher than 80% in the 10 h electrolysis experiment (Fig. 5f), demonstrating that TPPDA-CoPor-COF has an acceptable electrochemical catalytic stability in spite of a decrease of the current density (~20%). The stability of TPPDA-CoPor-COF was further demonstrated by the almost unchanged XPS (Fig. S25†) and PXRD (Fig. S26†) data after 2 h and 10 h of electrocatalysis at −0.8 V. The SEM and TEM (Fig. S27†) images of TPPDA-CoPor-COF after 2 h and 10 h of electrolysis suggest that the layered morphology of the catalysts is retained well. The above results well disclose its good electrochemical catalytic stability.

Based on previous reports,[27,28] the high stability and performance of two-dimensional TPPDA-CoPor-COF motivated us to ultrasonically exfoliate the materials to further improve their catalytic activity. TPPDA-CoPor-COF was converted into TPPDA-CoPor-COF-NSs with a thin-layered morphology (Fig. S28†) and a thickness of ~7 nm as proved by atomic force microscopy (AFM) measurements (Fig. 6a and b). Almost identical PXRD curves indicated that the periodic structure of TPPDA-CoPor-COF was retained in the nanosheets after ultra-

sonic exfoliation (Fig. S29†). To evaluate the electrocatalytic CO_2RR performance of TPPDA-CoPor-COF-NSs, the same short- and long-term electrolysis tests were conducted (Fig. S30 and S31†), and the corresponding FE_{CO} and j_{CO} were calculated. The FE_{CO} values of TPPDA-CoPor-COF-NSs are above 90% in a wider range (−0.7 to −0.9 V) than those of TPPDA-CoPor-COF (Fig. 6c). The maximum FE_{CO} value of TPPDA-CoPor-COF-NSs is 92% at −0.7 V and the j_{CO} reaches up to −29.2 mA cm^{-2} at −1.0 V (Fig. 6d), which are higher than those of the unexfoliated one. The promoted CO_2RR performance of TPPDA-CoPor-COF-NSs could be attributed to the more exposed Co active sites.[27,28] Besides, a 10 h chrono-amperometric test of the nanosheets at −0.7 V was carried out. Same as the unexfoliated one, the corresponding FE_{CO} can be kept above 80% in the whole electrolysis process as well (Fig. S29†), indicating that TPPDA-CoPor-COF-NSs also have tolerable electrochemical catalytic stability, although accompanied by a certain degree of current density attenuation.

DFT calculations

The frontier molecular orbitals of the repeat unit in TPPDA-MPor-COFs were calculated by DFT calculations (Fig. S32 and S33†). The HOMO is located on the TPPDA moiety, while the LUMO is on the MPor moiety, implying the electronic donor–acceptor configuration of the two COFs, which usually means decreased band gaps and enhanced electron transfer properties for organic semiconductors.

To understand the superior CO_2RR performance of TPPDA-CoPor-COF, the CO_2RR and HER mechanisms were calculated together with those of TPPDA-NiPor-COF and the CoPor monomer (Fig. 7a–c). According to the calculated relative free energies, the rate determining steps (RDSs) for the CO_2RR and HER are the formation of *COOH and *H inter-
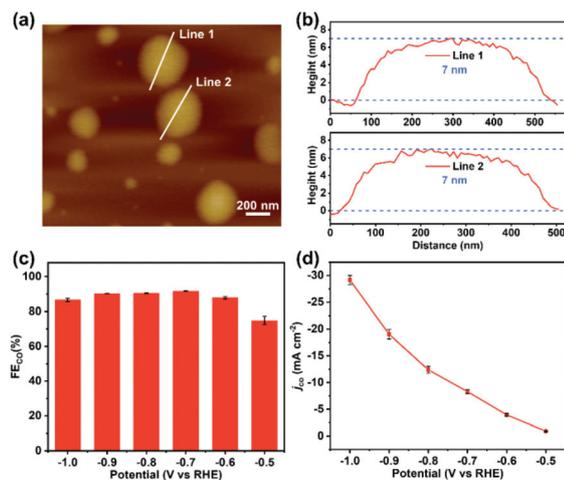

Fig. 6 (a) The atomic force microscopy topographical image. (b) Corresponding height curves of (a). (c) FE_{CO} of TPPDA-CoPor-COF-NSs. (d) Lasting stability test of TPPDA-CoPor-COF-NSs at −0.7 V.

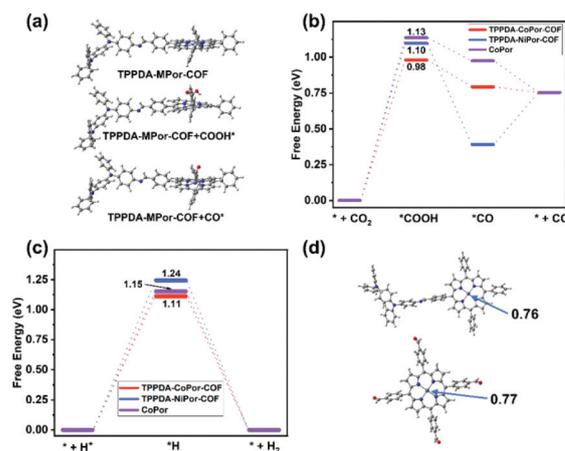**Fig. 7** (a) The proposed mechanism of the electrocatalytic CO_2RR for TPPDA-MPor-COFs. (b) The calculated energy diagrams of CO_2 reduction to CO and (c) the calculated energy diagrams of the HER for TPPDA-MPor-COFs and CoPor. (d) The Mulliken charge of the Co site in TPPDA-CoPor-COF and CoPor.

3220 | *Inorg. Chem. Front.*, 2022, **9**, 3217–3223

This journal is © the Partner Organisations 2022

mediates, respectively.[49] The ΔG_{RDS} values of the CO_2RR for TPPDA-CoPor-COF (0.98 eV), TPPDA-NiPor-COF (1.10 eV) and CoPor (1.13 eV) are all lower than the respective ΔG_{RDS} values of the HER (1.11 eV, 1.24 eV, and 1.15 eV), indicating their preferable CO_2RR activity. TPPDA-CoPor-COF exhibits dramatically reduced ΔG_{RDS} of the CO_2RR relative to the CoPor monomer, suggesting that the introduction of the TPPDA unit and the formation of COFs could promote the CO_2RR activity of the CoPor core. Mulliken population and frontier orbital analyses afforded consistent results (Fig. 7d and Fig. S34†).[50] The Mulliken atom charge of the Co sites in TPPDA-CoPor-COF (0.76) is lower than that in the CoPor monomer (0.77), indicating the more electron-rich environment of the Co atom in TPPDA-CoPor-COF. The LUMO level of TPPDA-CoPor is −2.29 eV, which is higher than that of CoPor (−2.42 eV), suggesting the higher reducibility of TPPDA-CoPor-COF in the electrocatalytic process. TPPDA-NiPor-COF displays a higher ΔG_{RDS} of the CO_2RR than that of TPPDA-CoPor-COF, suggesting the harder formation of *COOH intermediates on TPPDA-NiPor-COF. Furthermore, the desorption of CO from TPPDA-NiPor-COF (*CO → *+CO) is endothermic, while this step for TPPDA-CoPor-COF is exothermic (Fig. 7b), indicating that the Co site shows superior CO_2RR activity than the Ni site in the COFs, which is consistent with the experimental results.

Conclusions

In summary, metalloporphyrin- and TPPDA-based two-dimensional COFs were explored for the electrocatalytic CO_2RR in the H-cell. The obtained TPPDA-CoPor-COF exhibits a high FE_{CO} of 87–90% in the range of −0.6 to −0.9 V and a maximum j_{CO} of −22.2 mA cm^{-2} at −1.0 V. The exfoliated TPPDA-CoPor-COF-NSs show further improved FE_{CO} and j_{CO} than the as-prepared TPPDA-CoPor-COF. DFT calculations reveal that the integration of the TPPDA block enhances the electron transfer ability of TPPDA-MPor-COFs and reduces the CO_2RR energy barrier of the CoPor core. This work would be conducive to the rationally designed novel COF-based electrocatalysts towards the CO_2RR.

Author contributions

Lei Gong, Baotong Chen, Ying Gao and Yinhai Wang performed experiments under the guidance of Yongzhong Bian and Jianzhuang Jiang. Dongdong Qi, Bin Han, Chenxiang Lin and Baoqiu Yu provided assistance for data acquisition and analysis. All authors discussed the results and commented on the manuscript.

Conflicts of interest

There are no conflicts to declare.

Acknowledgements

Notes and references

1 Z. Fu, X. Wang, A. M. Gardner, X. Wang, S. Y. Chong, G. Neri, A. J. Cowan, L. Liu, X. Li, A. Vogel, R. Clowes, M. Bilton, L. Chen, R. S. Sprick and A. I. Cooper, A stable covalent organic framework for photocatalytic carbon dioxide reduction, *Chem. Sci.*, 2020, **11**, 543–550.

2 Y. Gong, W. Zhong, Y. Li, Y. Qiu, L. Zheng, J. Jiang and H. Jiang, Regulating Photocatalysis by Spin-State Manipulation of Cobalt in Covalent Organic Frameworks, *J. Am. Chem. Soc.*, 2020, **142**, 16723–16731.

3 W. Liu, X. Li, C. Wang, H. Pan, W. Liu, K. Wang, Q. Zeng, R. Wang and J. Jiang, A Scalable General Synthetic Approach toward Ultrathin Imine-Linked Two-Dimensional Covalent Organic Framework Nanosheets for Photocatalytic CO_2 Reduction, *J. Am. Chem. Soc.*, 2019, **141**, 17431–17440.

4 S. Ren, D. Joulié, D. Salvatore, K. Torbensen, M. Wang, M. Robert and C. P. Berlinguette, Molecular electrocatalysts can mediate fast, selective CO2 reduction in a flow cell, *Science*, 2019, **365**, 367–369.

5 F. P. García De Arquer, C. Dinh, A. Ozden, J. Wicks, C. Mccallum, A. R. Kirmani, D. Nam, C. Gabardo, A. Seifitokaldani, X. Wang, Y. C. Li, F. Li, J. Edwards, L. J. Richter, S. J. Thorpe, D. Sinton and E. H. Sargent, CO_2 electrolysis to multicarbon products at activities greater than 1 A cm^{-2}, *Science*, 2020, **367**, 661–666.

6 Z. Liang, H. Wang, H. Zheng, W. Zhang and R. Cao, Porphyrin-based frameworks for oxygen electrocatalysis and catalytic reduction of carbon dioxide, *Chem. Soc. Rev.*, 2021, **50**, 2540–2581.

7 S. Kattel, P. Liu and J. G. Chen, Tuning Selectivity of CO_2 Hydrogenation Reactions at the Metal/Oxide Interface, *J. Am. Chem. Soc.*, 2017, **139**, 9739–9754.

8 N. M. Haegel, R. Margolis, T. Buonassisi, D. Feldman, A. Froitzheim, R. Garabedian, M. Green, S. Glunz, H. Henning, B. Holder, I. Kaizuka, B. Kroposki, K. Matsubara, S. Niki, K. Sakurai, R. A. Schindler, W. Tumas, E. R. Weber, G. Wilson, M. Woodhouse and S. Kurtz, Terawatt-scale photovoltaics: Trajectories and challenges, *Science*, 2017, **356**, 141–143.

9 S. Nitopi, E. Bertheussen, S. B. Scott, X. Liu, A. K. Engstfeld, S. Horch, B. Seger, I. E. L. Stephens, K. Chan, C. Hahn, J. K. Nørskov, T. F. Jaramillo and I. Chorkendorff, Progress and Perspectives of Electrochemical CO_2 Reduction on Copper in Aqueous Electrolyte, *Chem. Rev.*, 2019, **119**, 7610–7672.

This journal is © the Partner Organisations 2022

Inorg. Chem. Front., 2022, **9**, 3217–3223 | **3221**

10 E. E. Benson, C. P. Kubiak, A. J. Sathrum and J. M. Smieja, Electrocatalytic and homogeneous approaches to conversion of CO2 to liquid fuels, *Chem. Soc. Rev.*, 2009, **38**, 89–99.

11 R. Francke, B. Schille and M. Roemelt, Homogeneously Catalyzed Electroreduction of Carbon Dioxide-Methods, Mechanisms, and Catalysts, *Chem. Rev.*, 2018, **118**, 4631–4701.

12 X. Huang and Y. Zhang, Reticular materials for electrochemical reduction of CO2, *Coord. Chem. Rev.*, 2021, **427**, 213564.

13 Y. Wu, Z. Jiang, X. Lu, Y. Liang and H. Wang, Domino electroreduction of CO_2 to methanol on a molecular catalyst, *Nature*, 2019, **575**, 639–642.

14 W. Yang, J. Zhang, R. Si, L. Cao, D. Zhong and T. Lu, Efficient and steady production of 1:2 syngas (CO/H_2) by simultaneous electrochemical reduction of CO_2 and H_2O, *Inorg. Chem. Front.*, 2021, **8**, 1695–1701.

15 P. T. Smith, B. P. Benke, Z. Cao, Y. Kim, E. M. Nichols, K. Kim and C. J. Chang, Iron Porphyrins Embedded into a Supramolecular Porous Organic Cage for Electrochemical CO_2 Reduction in Water, *Angew. Chem., Int. Ed.*, 2018, **57**, 9684–9688.

16 J. Han, P. An, S. Liu, X. Zhang, D. Wang, Y. Yuan, J. Guo, X. Qiu, K. Hou, L. Shi, Y. Zhang, S. Zhao, C. Long and Z. Tang, Reordering d Orbital Energies of Single–Site Catalysts for CO_2 Electroreduction, *Angew. Chem., Int. Ed.*, 2019, **58**, 12711–12716.

17 Y. Zhang, C. Cao, X. Wu and Q. Zhu, Three-dimensional porous copper-decorated bismuth-based nanofoam for boosting the electrochemical reduction of CO_2 to formate, *Inorg. Chem. Front.*, 2021, **8**, 2461–2467.

18 S. Gao, Y. Lin, X. Jiao, Y. Sun, Q. Luo, W. Zhang, D. Li, J. Yang and Y. Xie, Partially oxidized atomic cobalt layers for carbon dioxide electroreduction to liquid fuel, *Nature*, 2016, **529**, 68–71.

19 X. Zhang, Y. Wang, M. Gu, M. Wang, Z. Zhang, W. Pan, Z. Jiang, H. Zheng, M. Lucero, H. Wang, G. E. Sterbinsky, Q. Ma, Y. Wang, Z. Feng, J. Li, H. Dai and Y. Liang, Molecular engineering of dispersed nickel phthalocyanines on carbon nanotubes for selective CO_2 reduction, *Nat. Energy*, 2020, **5**, 684–692.

20 P. Shao, L. Yi, S. Chen, T. Zhou and J. Zhang, Metal-organic frameworks for electrochemical reduction of carbon dioxide: The role of metal centers, *J. Energy Chem.*, 2020, **40**, 156–170.

21 E. Zhang, T. Wang, K. Yu, J. Liu, W. Chen, A. Li, H. Rong, R. Lin, S. Ji, X. Zheng, Y. Wang, L. Zheng, C. Chen, D. Wang, J. Zhang and Y. Li, Bismuth Single Atoms Resulting from Transformation of Metal-Organic Frameworks and Their Use as Electrocatalysts for CO_2 Reduction, *J. Am. Chem. Soc.*, 2019, **141**, 16569–16573.

22 H. Zhong, M. Ghorbani-Asl, K. H. Ly, J. Zhang, J. Ge, M. Wang, Z. Liao, D. Makarov, E. Zschech, E. Brunner, I. M. Weidinger, J. Zhang, A. V. Krasheninnikov, S. Kaskel, R. Dong and X. Feng, Synergistic electroreduction of

carbon dioxide to carbon monoxide on bimetallic layered conjugated metal-organic frameworks, *Nat. Commun.*, 2020, **11**, 1409.

23 J. Li, X. Jing, Q. Li, S. Li, X. Gao, X. Feng and B. Wang, Bulk COFs and COF nanosheets for electrochemical energy storage and conversion, *Chem. Soc. Rev.*, 2020, **49**, 3364–3565.

24 Y. Yusran, Q. Fang and V. Valtchev, Electroactive Covalent Organic Frameworks: Design, Synthesis, and Applications, *Adv. Mater.*, 2020, **32**, 2002038.

25 S. Lin, C. S. Diercks, Y. B. Zhang, N. Kornienko, E. M. Nichols, Y. Zhao, A. R. Paris, D. Kim, P. Yang, O. M. Yaghi and C. J. Chang, Covalent organic frameworks comprising cobalt porphyrins for catalytic CO_2 reduction in water, *Science*, 2015, **349**, 1208–1213.

26 H. Liu, J. Chu, Z. Yin, X. Cai, L. Zhuang and H. Deng, Covalent Organic Frameworks Linked by Amine Bonding for Concerted Electrochemical Reduction of CO_2, *Chem*, 2018, **4**, 1696–1709.

27 H. Zhu, M. Lu, Y. Wang, S. Yao, M. Zhang, Y. Kan, J. Liu, Y. Chen, S. Li and Y. Lan, Efficient electron transmission in covalent organic framework nanosheets for highly active electrocatalytic carbon dioxide reduction, *Nat. Commun.*, 2020, **11**, 497.

28 Q. Wu, M. J. Mao, Q. J. Wu, J. Liang, Y. B. Huang and R. Cao, Construction of Donor-Acceptor Heterojunctions in Covalent Organic Framework for Enhanced CO2 Electroreduction, *Small*, 2021, **17**, 2004933.

29 S. An, C. Lu, Q. Xu, C. Lian, C. Peng, J. Hu, X. Zhuang and H. Liu, Constructing Catalytic Crown Ether-Based Covalent Organic Frameworks for Electroreduction of CO_2, *ACS Energy Lett.*, 2021, **6**, 3496–3502.

30 E. M. Johnson, R. Haiges and S. C. Marinescu, Covalent-Organic Frameworks Composed of Rhenium Bipyridine and Metal Porphyrins: Designing Heterobimetallic Frameworks with Two Distinct Metal Sites, *ACS Appl. Mater. Interfaces*, 2018, **10**, 37919–37927.

31 P. L. Cheung, S. K. Lee and C. P. Kubiak, Facile Solvent-Free Synthesis of Thin Iron Porphyrin COFs on Carbon Cloth Electrodes for CO_2 Reduction, *Chem. Mater.*, 2019, **31**, 1908–1919.

32 N. Huang, K. H. Lee, Y. Yue, X. Xu, S. Irle, Q. Jiang and D. Jiang, A Stable and Conductive Metallophthalocyanine Framework for Electrocatalytic Carbon Dioxide Reduction in Water, *Angew. Chem., Int. Ed.*, 2020, **59**, 16587–16593.

33 B. Han, X. Ding, B. Yu, H. Wu, W. Zhou, W. Liu, C. Wei, B. Chen, D. Qi, H. Wang, K. Wang, Y. Chen, B. Chen and J. Jiang, Two-Dimensional Covalent Organic Frameworks with Cobalt(ɪɪ)-Phthalocyanine Sites for Efficient Electrocatalytic Carbon Dioxide Reduction, *J. Am. Chem. Soc.*, 2021, **143**, 7104–7113.

34 Y. Yue, P. Cai, K. Xu, H. Li, H. Chen, H. Zhou and N. Huang, Stable Bimetallic Polyphthalocyanine Covalent Organic Frameworks as Superior Electrocatalysts, *J. Am. Chem. Soc.*, 2021, **143**, 18052–18060.

3222 | *Inorg. Chem. Front.*, 2022, **9**, 3217–3223

This journal is © the Partner Organisations 2022

35 Q. Hao, Z. J. Li, B. Bai, X. Zhang, Y. W. Zhong, L. J. Wan and D. Wang, A Covalent Organic Framework Film for Three–State Near–Infrared Electrochromism and a Molecular Logic Gate, *Angew. Chem., Int. Ed.*, 2021, **60**, 12498–12503.

36 J. M. Rotter, R. Guntermann, M. Auth, A. Mähringer, A. Sperlich, V. Dyakonov, D. D. Medina and T. Bein, Highly conducting Wurster-type twisted covalent organic frameworks, *Chem. Sci.*, 2020, **11**, 12843–12853.

37 C. Krishnaraj, H. Sekhar Jena, L. Bourda, A. Laemont, P. Pachfule, J. Roeser, C. V. Chandran, S. Borgmans, S. M. J. Rogge, K. Leus, C. V. Stevens, J. A. Martens, V. Van Speybroeck, E. Breynaert, A. Thomas and P. Van Der Voort, Strongly Reducing (Diarylamino)benzene-Based Covalent Organic Framework for Metal-Free Visible Light Photocatalytic H$_2$O$_2$ Generation, *J. Am. Chem. Soc.*, 2020, **142**, 20107–20116.

38 F. Yu, W. Liu, S. Ke, M. Kurmoo, J. Zuo and Q. Zhang, Electrochromic two-dimensional covalent organic framework with a reversible dark-to-transparent switch, *Nat. Commun.*, 2020, **11**, 5534.

39 A. El-Mahdy, M. G. Mohamed, T. H. Mansoure, H. H. Yu, T. Chen and S. W. Kuo, Ultrastable tetraphenyl-*p*-phenylenediamine-based covalent organic frameworks as platforms for high-performance electrochemical supercapacitors, *Chem. Commun.*, 2019, **55**, 14890–14893.

40 S. Wan, F. Gándara, A. Asano, H. Furukawa, A. Saeki, S. K. Dey, L. Liao, M. W. Ambrogio, Y. Y. Botros, X. Duan, S. Seki, J. F. Stoddart and O. M. Yaghi, Covalent Organic Frameworks with High Charge Carrier Mobility, *Chem. Mater.*, 2011, **23**, 4094–4097.

41 T. W. Kim, S. Jun, Y. Ha, R. K. Yadav, A. Kumar, C. Yoo, I. Oh, H. Lim, J. W. Shin, R. Ryoo, H. Kim, J. Kim, J. Baeg and H. Ihee, Ultrafast charge transfer coupled with lattice phonons in two-dimensional covalent organic frameworks, *Nat. Commun.*, 2019, **10**, 1873.

42 T. Joshi, C. Chen, H. Li, C. S. Diercks, G. Wang, P. J. Waller, H. Li, J. L. Bredas, O. M. Yaghi and M. F. Crommie, Local Electronic Structure of Molecular Heterojunctions in a Single-Layer 2D Covalent Organic Framework, *Adv. Mater.*, 2019, **31**, 1805941.

43 V. Petříček, M. Dušek and L. Palatinus, Crystallographic Computing System JANA2006, *Zeitschrift für Kristallographie - Crystalline Materials*, 2014, **229**, 345–352.

44 Y. Zeng, R. Zou, Z. Luo, H. Zhang, X. Yao, X. Ma, R. Zou and Y. Zhao, Covalent Organic Frameworks Formed with Two Types of Covalent Bonds Based on Orthogonal Reactions, *J. Am. Chem. Soc.*, 2015, **137**, 1020–1023.

45 C. Lin, X. Liu, B. Yu, C. Han, L. Gong, C. Wang, Y. Gao, Y. Bian and J. Jiang, Rational Modification of Two-Dimensional Donor–Acceptor Covalent Organic Frameworks for Enhanced Visible Light Photocatalytic Activity, *ACS Appl. Mater. Interfaces*, 2021, **13**, 27041–27048.

46 L. Hernan, J. Morales, L. Sanchez, J. L. Tirado, J. P. Espinos and A. R. Gonzalez Elipe, Diffraction and XPS Studies of Misfit Layer Chalcogenides Intercalated with Cobaltocene, *Chem. Mater.*, 1995, **7**, 1576–1582.

47 G. J. Colpas, M. J. Maroney, C. Bagyinka, M. Kumar, W. S. Willis, S. L. Suib, P. K. Mascharak and N. Baidya, X-ray spectroscopic studies of nickel complexes, with application to the structure of nickel sites in hydrogenases, *Inorg. Chem.*, 1991, **30**, 920–928.

48 N. Li, W. Lu, K. Pei and W. Chen, Interfacial peroxidase-like catalytic activity of surface-immobilized cobalt phthalocyanine on multiwall carbon nanotubes, *RSC Adv.*, 2015, **5**, 9374–9380.

49 A. A. Peterson, F. Abild-Pedersen, F. Studt, J. Rossmeisl and J. K. Nørskov, How copper catalyzes the electroreduction of carbon dioxide into hydrocarbon fuels, *Energy Environ. Sci.*, 2010, **3**, 1311.

50 J. D. Yi, D. H. Si, R. Xie, Q. Yin, M. D. Zhang, Q. Wu, G. L. Chai, Y. B. Huang and R. Cao, Conductive Two-Dimensional Phthalocyanine-based Metal-Organic Framework Nanosheets for Efficient Electroreduction of CO$_2$, *Angew. Chem., Int. Ed.*, 2021, **60**, 17108–17114.

This journal is © the Partner Organisations 2022

Inorg. Chem. Front., 2022, **9**, 3217–3223 | **3223**